Expansion and fragmentation of liquid metal droplet by a short laser pulse

S. Yu. Grigoryev,[1,2,*] B. V. Lakatosh,[3] M. S. Krivokorytov,[4,5] V. V. Zhakhovsky,[1,2,†]
S. A. Dyachkov,[1,2,3,6] D. K. Ilnitsky,[1,2] K. P. Migdal,[1,2] N. A. Inogamov,[1,2] A. Yu. Vinokhodov,[5]
V. O. Kompanets,[4] Yu. V. Sidelnikov,[4] V. M. Krivtsun,[4,5] K. N. Koshelev,[4,5] and V. V. Medvedev[3,4,‡]

[1] *Dukhov Research Institute of Automatics, Sushchevskaya st. 22, 127055 Moscow, Russia*
[2] *Landau Institute for Theoretical Physics, RAS, Akademika Semenova av. 1-A, 142432 Chernogolovka, Moscow Region, Russia*
[3] *Moscow Institute of Physics and Technology, Institutskiy per. 9, 141701 Dolgoprudny, Moscow region, Russia*
[4] *Institute for Spectroscopy, RAS, Fizicheskaya st. 5, Troitsk, Moscow region, Russia*
[5] *EUV Labs, Sirenevy blvd. 1, Troitsk, Moscow region, Russia*
[6] *Joint Institute for High Temperatures, RAS, Izhorskaya st. 13/2, 125412 Moscow, Russia*

(Dated: October 17, 2018)

We report an experimental and numerical study of the fragmentation mechanisms of a micrometer-sized metal droplet irradiated by ultrashort laser pulses. The results of the experiment show that the fast one-side heating of such a droplet may lead to either symmetric or asymmetric expansion followed by different fragmentation scenarios. To unveil the underlying processes leading to fragmentation we perform simulations of liquid-tin droplet expansion produced by the initial conditions similar to those in experiment using the smoothed particle hydrodynamics (SPH) method. Simulations demonstrate that a thin heated surface layer generates an ultrashort shock wave propagating from the frontal side to the rear side of a droplet. Convergence of such a shock wave followed by an unloading tail to the droplet center results in cavitation of material inside the central zone caused by the strong tensile stress. Reflection of a shock wave from the rear side of a droplet produces another region of highly stretched material where spallation may occur producing a thin spall layer moving with a velocity higher than the expansion rate of the liquid shell around the central cavity. It is shown both experimentally and numerically that the threshold laser intensity necessary for the spallation is higher than the threshold required to induce cavitation nearby the droplet center. Thus, the regime of asymmetrical expansion is realized if the laser intensity exceeds the rear-side spallation threshold. The transverse and longitudinal expansion velocities obtained in SPH simulations of different expansion regimes are agreed well with our experimental data.

INTRODUCTION

Fragmentation of liquid droplets underlies a wide range of technological processes including mass spectrometry, liquid fuel dispersion systems, coating deposition, and fabrication of microstructures. In addition, the processes of droplet fragmentation are observed in nature [1] what causes an interest in investigating fragmentation mechanisms.

An unperturbed liquid droplet is a hydrodynamically stable object. Fragmentation occurs only as a result of a sufficiently strong external influence. Thus, the fragmentation process strongly depends both on the mechanism of an external action and on the properties of a droplet itself. This incorporates a wide range of fragmentation mechanisms which are observed in external electric and magnetic fields [2, 3], during interaction with a gas jet [4], in collisions with a solid obstacle [5], in collisions of droplets with one another [6], or under the action of a laser pulse [7].

The most intense fragmentation occurs under the influence of shock waves. A shock wave can propagate in an extrenal environment [8, 9] or be formed within a droplet by applying an external force on a time scale substantially shorter than the time of sound propagation through it. The latter occurs when droplets collide with a solid surface at very high velocities [10] or when a droplet is irradiated by short laser pulses [11–17]. Laser energy can be released both in the volume of a droplet [11, 12] and at its surface [13] what depends on the optical properties of a material at a laser wavelength. In the last case the fragmentation scenario may vary.

The problem of interaction of a laser pulse with a droplet has attained practical interest during the development of extreme ultraviolet (EUV) sources used in the next-generation industrial lithography [18–20]. It was found that irradiation of a tens-micrometer sized liquid-metal tin droplet by two successive laser pulses produces plasma which emit photons in the EUV range [18, 19, 21]. The first pulse (known as the "pre-pulse") serves to optimize the target by deforming [22] or even fragmenting it [21]. The second pulse (known as the "main pulse") heats the material to a high-temperature plasma state. Fujimoto et al. [18] demonstrated that the highest efficiency of the main pulse energy conversion into the EUV is achieved with the use of picosecond pre-pulses.

Our previous work [13, 15] presented a phenomenological description of fragmentation of liquid-metal droplets exposed to Ti:sapphire laser pulses. We also discussed possible physical fragmentation mechanisms associated with the propagation of shock waves in spherical sam-

* grigorev@phystech.edu
† 6asi1z@gmail.com
‡ medvedev@phystech.edu

ples [14]. In the present paper we report the systematic study of a droplet response to short laser pulses of various energies (intensities). Using the method of instantaneous shadow photography, we observe that a droplet subjected to laser pulses undergoes a strong expansion with the formation of internal cavities. This means that a uniform droplet takes the form of a soap bubble with a liquid-metal shell. At high intensities the formation of two cavities is clearly observed: one (front) cavity is closer to the side of a droplet irradiated by a laser pulse, and the other (rear) cavity appears at the opposite side. When the laser intensity decreases, the expansion rate of the rear cavity falls considerably faster than that of the front cavity. At the certain intensity the rear cavity disappears completely. In addition, a variation in the intensity of laser pulses affecting a droplet changes the fragmentation scenario qualitatively. At high intensities a liquid-metal shell is fragmented during expansion. At low intensities, when the rear cavity disappears, the expansion of a shell becomes limited, and it begins to shrink due to surface tension. In this case, the shell finally breaks apart on internal nonuniformities what results in the formation of jets and smaller droplets.

To understand the mechanism of the cavities formation within a droplet, we perform the detailed numerical simulations of a shock waves propagation induced by a laser pulse. The smoothed particle hydrodynamics (SPH) method is used as the most appropriate one to model flows with the loss of continuity and fragmentation. The results of the numerical study clearly demonstrate that the formation of cavities is a result of exceeding the spall strength of liquid under the action of strong tensile stresses in the unloading tail following the shock front.

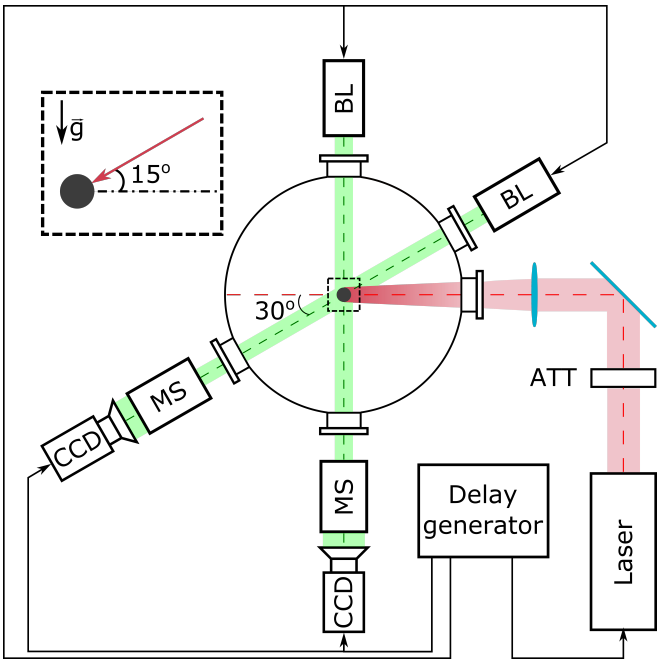

Figure 1. The experimental setup scheme to study the liquid-metal droplet fragmentation by short laser pulses: (Laser) Ti:sapphire laser; (CCD) CCD camera; (MS) microscope; (ATT) attenuator; (BL) pulsed back illumination. Droplets move perpendicular to the plane of the figure. The Ti:sapphire laser beam comes at 15° to the plane of the figure.

EXPERIMENTAL SETUP

The experimental setup scheme is shown in Fig. 1. The experiment is performed in the vacuum chamber where the residual gas pressure is less than 10^{-2} Pa. The Sn–In liquid-alloy targets (in a mass proportion of 52%–48%) are used instead of the pure tin ones to decrease the melting temperature from 232° C (Sn) to 119° C (Sn–In). That greatly simplifies the experiment while tin component provides the required plasma for the EUV light generation. To produce targets we use the previously developed droplet generator [15] ensuring the Plateau–Rayleigh instability to split jets into droplets. The generator is synchronized with laser pulses what provides an accurate irradiation of a target. The laser beam is focused on a free-flying drop of liquid metal at a sufficient distance from the generator nozzle to guarantee the natural oscillations of a droplet are damped. The radii of the droplets generated throughout the experiments are almost identical and amount to $24.5 \pm 0.8\,\mu$m.

Figure 1 shows that the incident laser beam is 15° with the horizontal plane. We use the Ti:sapphire laser ($\lambda = 780 - 820$ nm) with the fixed pulse duration $\tau = 800$ fs and the Gaussian intensity profile in the focal plane. The size of the focal spot defined as the full width at the half-height is $D_L = 60\,\mu$m. The laser pulse energy (E_L) varies in the experiments from 0.08 to 1.66 mJ. The corresponding intensity of the laser pulses, which is defined as $I_L = 4E_L/(\tau\pi D_L^2)$, varies in the range $(0.4 - 8.0) \times 10^{13}$ W/cm^2.

The droplet response to the focused laser pulse is recorded using the shadow photograph method. CCD cameras are directed perpendicular to a drop fall with the 30° angle to the horizontal projection of the laser beam (Fig. 1). To resolve small droplets the cameras are equipped with microscopes. The 30-ns pulsed laser is mounted opposite each camera for back illumination what determines exposure. The droplet velocity is about 10 m/s, so that images can be considered instantaneous with a good accuracy. By varying the delay between the camera and the Ti:sapphire laser pulse, it is possible to obtain images of the droplet shape evolution at its various stages. To ensure accuracy we perform measurements with 100 samples.

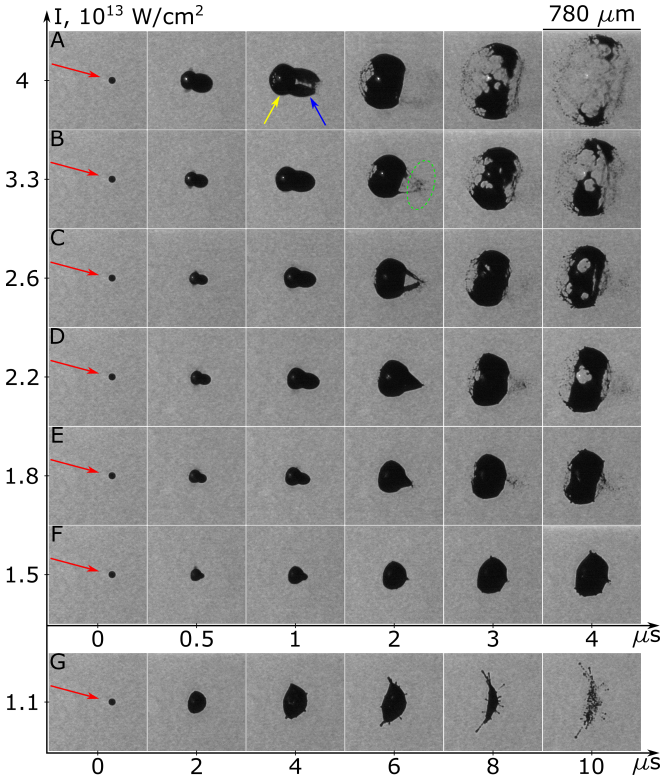

Figure 2. The side views of the target shape evolution for the different laser pulse intensities presented on the vertical axis. The horizontal axes shows the time delays relative to the laser pulse. The red arrow indicates the direction of laser beam at an angle of 30°; the yellow and blue arrows show the central and rear-side shells, respectively. The green ellipse identifies the cloud of smaller droplets formed after the fragmentation of the rear-side shell. The dimensionless time is $t^* = tc/R = t/[10\,\text{ns}]$.

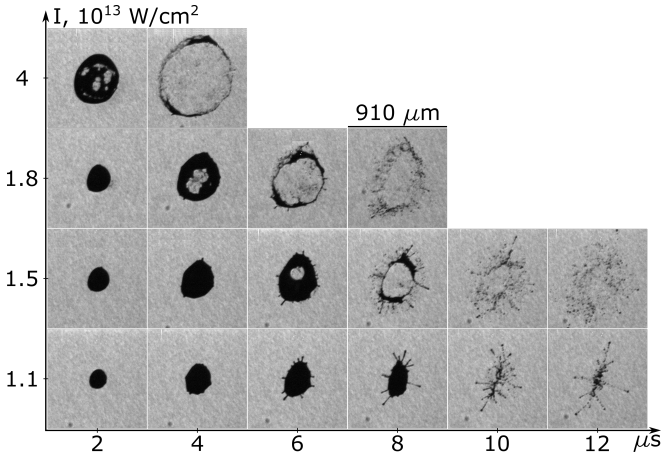

Figure 3. Rear-side views of the target shape evolution for different laser pulse intensities presented on the vertical axis. The horizontal axes indicate a frame delay relative to the laser pulse.

EVOLUTION OF DROPLET SHAPE OBSERVED IN EXPERIMENTS

The obtained shadowgraphs of the time evolution of liquid-metal droplets, which are subjected to short laser pulses, are ordered by the applied laser intensity I_L (Fig. 2). The range of laser intensities varies from 1.1×10^{13} to $4.0 \times 10^{13}\,\text{W/cm}^2$. The observed expansion and fragmentation process of a liquid-metal droplet qualitatively depends on a laser pulse intensity focused on it.

Our detailed analysis begins with the droplet response to the most intense laser pulse with $I_L = 4 \times 10^{13}\,\text{W/cm}^2$ shown in Fig. 2A. One should notice that the evolution of the droplet shape subjected to a more intense laser pulses $I_L \geq 4 \times 10^{13}\,\text{W/cm}^2$ has not new qualitative features except for an increase in the expansion rate. This scenario persists even with a slight change in the other parameters of the experiment, i.e. the size of the droplet, the size of the laser focal spot, etc. A similar regime of the liquid-metal droplet response to the action of a femtosecond laser pulse has already been described in detail in our previous paper [13]. Fig. 2A shows that after the action of the laser pulse the droplet asymmetrically expands over time, so that the droplet volume increases tenfold in 500 ns. As the mass of the droplet conserves, this expansion can be explained by the formation of two cavities within the droplet. Below, the first cavity arising in the center of the droplet is surrounded by the front shell (yellow arrow in Fig. 2A) and the second cavity emerging at the rear-side surface is surrounded by the rear shell (blue arrow in Fig. 2A). It is seen that both shells expand and eventually fragment over time. However, the rear-side shell fragments faster than the front shell. Thus, 2 μs after the action of the laser pulse, the rear shell is completely fragmented, whereas the front shell still remains intact.

A decrease in the laser pulse intensity leads to a decrease in the shells expansion rate and a change in their geometry. We noticed that under irradiation with $I_L \geq 4 \times 10^{13}\,\text{W/cm}^2$ the rear-side shell expands until fragmentation. However, with the decrease in intensity the shape of the rear shell gradually changes from the elongated ellipsoid into the cone-like form (Figs. 2B–2E). Finally, the rear shell also becomes fragmented, but the process develops in a different scenario. The collapse occurs due to the shell narrowing around the laser pulse direction, not to the expansion.

The decrease in the laser intensity down to $I_L = 1.5 \times 10^{13}\,\text{W/cm}^2$ (Fig. 2F) leads to the considerable shrink in the rear shell size, the further intensity decrease to $I_L = 1.1 \times 10^{13}\,\text{W/cm}^2$—to the rear shell disappearance (Fig. 2G). Nevertheless, the front shell is formed, but under the laser energy decrease its expansion becomes limited: after $\sim 6\,\mu$s from the laser irradiation the shell also begins to collapse.

It is also worth noting that at low intensities, starting at $\sim 4\,\mu$s, convexities appear on a droplet surface which then evolve into jets. These convexities are ob-

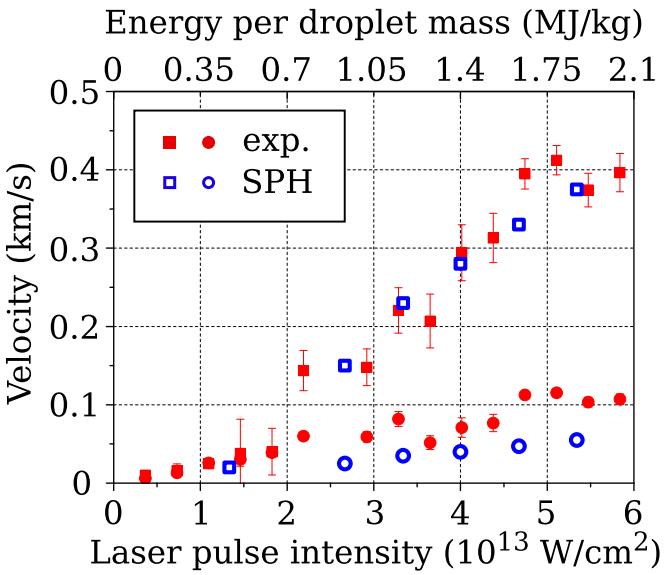

Figure 4. Expansion velocities of the central shell (circles) and rear-side shell (squares) as functions of laser pulse intensity (low axis) or the total absorbed energy per droplet mass (top axis). Red symbols correspond to the experimental data, and the blue ones show simulation data. The top axis is linked to the low one via the absorption coefficient of 0.125.

served even at $I_L \leq 1.5\times10^{13}$ W/cm^2 (Figs. 2F, 2G). The morphology of the expansion of fragmentation products in later times also changes: it becomes flatter in comparison to the results obtained at high-intensity laser pulses (Figs. 2A, 2G).

A change in the morphology of the fragmented droplet at low laser intensities, which is the damping of the rear shell formation, is also observed in the projection perpendicular to the laser beam. Figure 3 shows that for any laser intensity the expansion of a droplet is symmetric in this projection at earlier stages. But the later fragmentation scenario is changing. At $I_L \geq 1.8 \times 10^{13}$ W/cm^2 we observe the formation of a ring; at $I_L = 1.5\times10^{13}$ W/cm^2 jets are formed on the ring; and at $I_L = 1.1\times10^{13}$ W/cm^2 the ring does not appear at all: only jets are observed.

At late stages the dispersed fragments of a droplet continue to move by inertia. Their size distribution lies within a range of several micrometers or less. The velocity of fragments movement can be estimated from the expansion rates of the shells in the corresponding directions. The results of measuring the characteristic expansion rates of the shells along and perpendicular to the laser beam are shown in Fig. 4. One can notice that the shell expansion rates depend on the laser pulse intensity. It is interesting that the expansion rate of the rear shell along the laser beams reaches 500 m/s at $I_L = 7.3 \times 10^{13}$ W/cm^2, while the expansion rate of the front shell perpendicular to the laser beam is much less at the same intensity and reaches only 130 m/s. Fig. 4 also shows that at $I_L \leq 1.1 \times 10^{13}$ W/cm^2 the front and rear shells expansion rates coincide what indicates the rear shell disappearance.

SIMULATION SETUP

Equations of material motion

The droplets out of tin are simulated using a model of continuous compressible material. Its evolution is determined by the mass, momentum, and energy conservation equations:

$$\dot{\rho} + \rho \nabla \cdot \mathbf{U} = 0, \tag{1}$$

$$\rho \dot{\mathbf{U}} + \nabla P = 0, \tag{2}$$

$$\rho \dot{E} + \nabla \cdot (P\mathbf{U}) = q(\mathbf{r}, t), \tag{3}$$

where ρ and $\mathbf{U}$ are the density and the velocity of material, respectively; P is the hydrostatic pressure, which is determined from the equation of state; $E = e + \mathbf{U}^2/2$ is the total specific energy consisting of the internal and kinetic specific energies; and $q(\mathbf{r}, t)$ is the volumetric heat source which emulates the heating profile produced by laser irradiation and electron heat diffusion.

The reduced system of Eqs. (1)–(3) completed by the equation of state is solved during the simulation of droplet expansion and fragmentation by laser pulses using the SPH method [23]. The basic idea of SPH is to represent continuous material by lagrangian particles. In contrast to conventional grid methods here the governing equations are represented in integral forms, after which a transition is performed from integration to summation over neighboring SPH particles within the "smoothing radius". The usage of the Riemann solver at an interparticle contact [24, 25] to obtain the contact pressure and velocity provides a good accuracy in simulation of shock-wave phenomena. Moreover, simulation of discontinuities, which may result from the tensile stresses applied to material, is performed in a natural way without special algorithms for handling complex boundaries. The movement of free external and internal boundaries and surfaces can be directly tracked and compared to the experimental ones.

SPH simulations are performed using our in-house parallel code CSPH-VD^3, which utilizes the dynamic domain decomposition of material between the Voronoi subdomains and an automatic load balancing algorithm [26].

Equation of state for liquid tin

The system of Eqs. (1)–(3) is enclosed with an equation of state which couples the hydrostatic pressure, the density, and the internal energy. Unlike the experiment the pure liquid tin is used in our simulation instead of liquid-metal tin–indium alloy. Indium and tin have the close thermomechanical characteristics: the difference in the densities of liquid indium and tin is less than 1%

Table I. Properties of liquid tin.

Mechanical properties	Value
Initial density ρ_0, kg/m^3	6824
Compression modulus B, GPa	37.7
Specific heat C_v, J/(kgK)	227
Equation of state parameters	
Parameter Γ	1.486
Parameter c, km/s	2.45
Parameter s	1.45

(7030 kg/m^3 and 6980 kg/m^3, respectively) [27, 28]; the sound velocities are 2.59 and 2.49 km/s, respectively in In and Sn [29]; the surface tension of these materials is almost the same and equals to 0.55 N/m [30]. Thus, the material motion produced in Sn, including a shock-wave propagation, will be almost identical to that in In and Sn-In alloy.

We use the Mie–Grüneisen equation of state for liquid tin:

$$P = P(\rho, e) = P_r + \Gamma\rho(e - e_r), \tag{4}$$

where Γ is the Grüneisen parameter, and P_r and e_r are the reference pressure and the specific energy for which the shock Hugoniot is often used. The latter can be defined using the shock velocity u_s as a function of material velocity u_p in a form of linear approximation $u_s = c+su_p$, where c is the bulk sound velocity in an uncompressed state (here liquid) and s is the parameter. Thus, the reference pressure and the specific energy take the forms:

$$P_r(\rho) = \rho_0 c^2 \frac{1-x}{[1-s(1-x)]^2}, \qquad e_r = \frac{P_r}{\rho}\frac{1-x}{2}, \tag{5}$$

where $x = \rho_0/\rho$ is the compression ratio. The used parameters for the equation of state of liquid tin are given in Table I.

Spall strength of liquid tin

Our initial simulations demonstrated that the propagation of a shock wave generated by laser irradiation results in material stretching strong enough for void formation inside the droplet due to high tensile stresses in a wave tail following the shock front. The cavitation threshold, as well as for spallation, is the exceeding of the spall strength of material for a given strain rate. At this condition the material responses by forming the voids with free internal boundaries. The choice of this terminology does not contradict the generally accepted definitions of these concepts and is used to explicitly separate the studied processes. Otherwise, we mean that the processes of cavitation and spallation have a single physical nature associated with the stress relaxation in response to the stretching of material.

The critical tensile stress (or spall strength) is not a property of the material in question, but depends on a nature of loading, in particular on the strain rate. The information about the spall strength in liquid tin is rather scarce. It is known that for most metals the spall strength in a material is greatly reduced after a transition from solid to liquid. Thus, the spall strength in liquid tin decreases by an order of magnitude: from 1.2 GPa in the solid state to 0.12 GPa in the molten state [31]. However, the spall strength increases with the strain rate: the experiment by Ashitkov et al. shows that the spall strength in liquid tin is about 1.9 GPa at the strain rate of 1.3×10^9 s^{-1} [32].

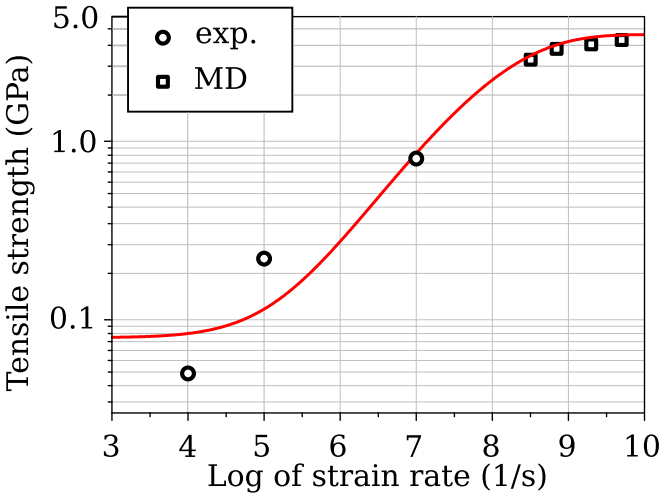

Figure 5. The spall strength of liquid tin as a function of the strain rate. The solid line is fitted to experimental data [33–35] (circles) and our molecular dynamic simulations at higher strain rates (squares).

To take into account the dependence of the spall strength from the strain rate, the strength curve was fitted to the known experimental data at moderated strain rates [33–35] and our molecular dynamics simulation results obtained at the very high strain rates as shown in Fig. 5. The fitted spall strength as a function of the strain rate $\sigma^* = 3.7(1 - 0.98\exp(-[\lg(\dot\varepsilon)/8.2]^{9.5}))$, where the strain rate $\dot\varepsilon$ is in s^{-1} units and σ^* is in GPa, is used in SPH simulations to trigger the cavitation process. Each pair of SPH particles for which the Riemann problem solution exceeds the spall strength at a given strain rate, the Riemann solution is substituted by the vacuum condition, which corresponds to the loss of interaction between those particles. This condition leads to a sudden relaxation of the local tensile stress to zero and a formation of voids in material.

Heating of surface layer

The energy of the femtosecond laser pulse is absorbed by free electrons in metals during a period that does not exceed ~ 100 fs (~ 10 fs for tin) what may be considered instantaneous in contrast to the 800-fs laser pulse dura-

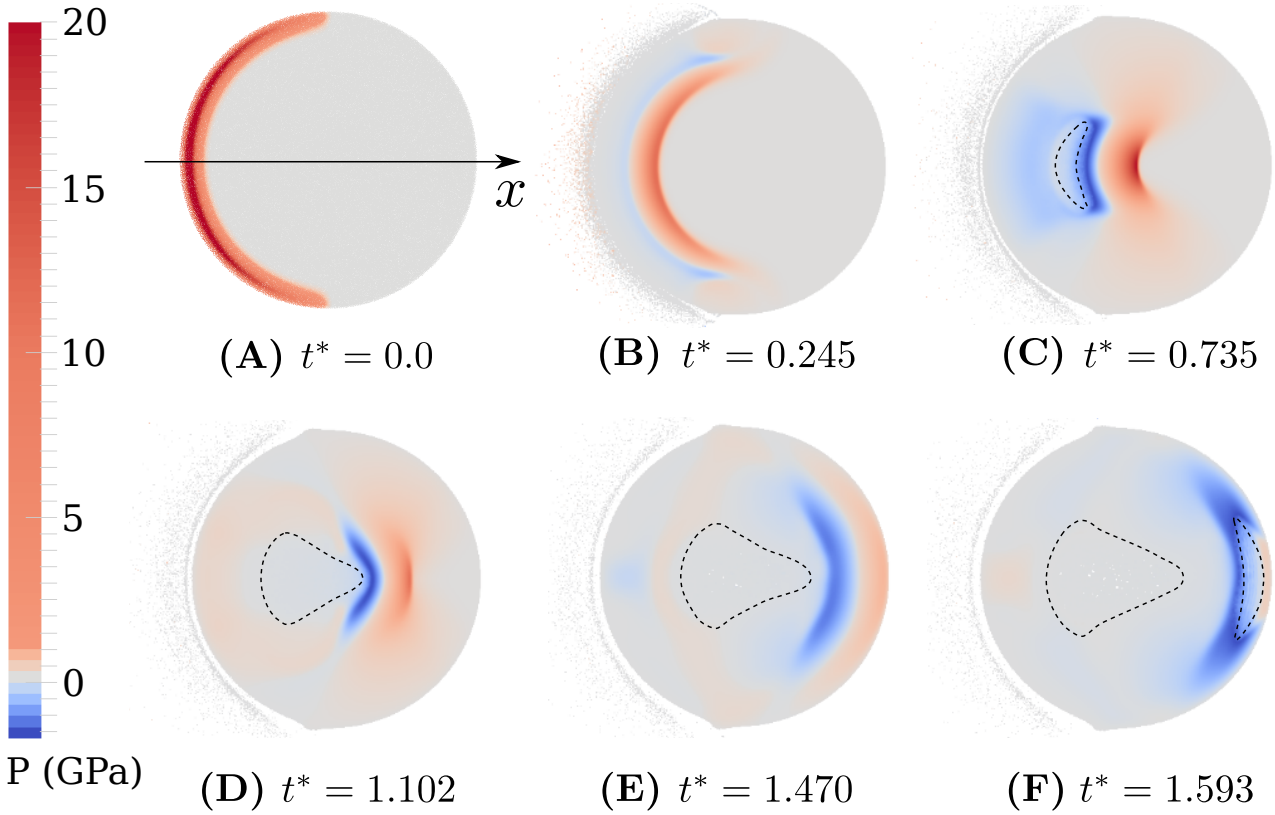

Figure 6. Pressure maps within a thin cross-section of droplet obtained at dimensionless times $t^* = ct/R$. The laser pulse propagates along the polar axis x and heats the left/frontal side of droplet. (A) the initial distribution of pressure after laser heating (maximum amplitude at the frontal focus, minimum amplitude near the equator); (B) broadening of the pressure wave profile and the formation of negative pressures in the wave tail during its propagation towards the droplet center; (C) increase of the compression and tensile stresses in the converging wave due to the focusing effect; the void formation after cavitation in the tensile tail nearby the droplet center; the cavitation zone is marked by the dashed curve; (D) decrease of the pressure in the diverging wave after passing the center of the droplet; the further growth of the central cavitation zone due to the propagation of the tensile tail; (E) the tensile stresses in the diverging wave become less than the spall strength and the cavitation stops at the central part of the droplet; (F) the spallation in liquid tin nearby the rear-side surface after the reflection of the arriving wave; the rear-side spallation zone is marked by another dashed curve. The corresponding evolution of the pressure distribution is shown in Supplemental Video at [URL will be given by publisher].

tion. Electron-ion energy transition leading to ion heating occurs due to the collisions between hot electrons and cold ions. The electron-ion relaxation completes within ~ 10 ps what results in an equilibrium temperature within the heated layer of a droplet. Our simulations do not take into account such relaxation processes: the laser energy absorption is modeled by setting the resulting internal energy distribution within the heated surface layer. The source term in the energy transport equation (3) is given by the Gaussian profile:

$$q(r,\theta,t) = \rho q_m \delta(t) e^{-(r-R)^2/\delta_h^2} \mathrm{H}\left(\pi/2-\theta\right)\cos\theta. \quad (6)$$

Here q_m is the maximal absorbed energy per unit mass, R is the radius of a droplet, r is the distance from the center of a droplet, $\delta(t)$ is the unit-impulse funtion, δ_h is the heated layer depth at which the absorbed energy is reduced by e times ($\delta_h = 70$ nm is used), and θ is the angle between the polar axis along the laser beam and the (r,θ)-point within the droplet. The Heaviside function $\mathrm{H}(\pi/2-\theta)$ determines the one-sided laser irradiation of a droplet from the left.

The heated depth δ_h, formed after the fast electron heat diffusion into the bulk during the electron-ion relaxation, is estimated using the two-temperature (2T) hydrodynamic model of a nonequilibrium system of electrons and ions. The calculation is carried out using the electron–ion exchange coefficients and the electronic thermal conductivity obtained from the ab-initio calculations of liquid tin at various electronic temperatures. The obtained equilibrium temperature profile takes a Gaussian shape with the corresponding heated depth δ_h between 60–80 nm in a wide range of absorbed fluences, which exceeds much the skin layer depth of the initial energy absorbtion $\delta \approx 8.5$ nm, see details in Appendicies A and B.

The angular dependence of the absorbed energy $q(\theta) \sim \cos\theta$ in (6) describes the inhomogeneous character of a

droplet heating. The absorbed energy varies depending on the incidence angle due to light reflection. It reaches a maximum on the plane surface irradiated at $\theta = 0$ and decreases for larger angles $\theta > 0$ for non-polarized light. A proper incident angle dependency for spherical geometry is the cosine function.

The direct 3D simulation of droplets with experimental sizes is resource consuming since the heated depth $\delta_h \sim 0.1\,\mu$m and the droplet radius $R \sim 25\,\mu$m differ by almost 3 orders of magnitude. Because we need at least 5-10 SPH particles to resolve the heated layer, the total number of SPH particles $\sim 10^{11}$ is required to make such a large droplet. This is why in the present paper we confine ourselves to smaller droplets with radii $R = 1,\, 2\,\mu$m. The possible scaling effects are discussed in the next Section.

SIMULATION RESULTS

The detailed analysis of processes within the irradiated liquid-metal droplet with the radius $R = 2\,\mu$m is based on SPH simulation results. The dynamic response of the droplet to the high-intensity experimental regime is illustrated in Fig. 6 by the series of 2D pressure maps. The absorption of the laser energy leads to the almost instantaneous heating of the heated layer with thickness of $\delta_h \sim 100\,$nm which is accompanied by an increase in pressure up to $\sim 30\,$GPa. One should notice that due to the introduced heating inhomogeneity $q(\theta)$ in (6), the pressure near the equatorial zone is reduced to zero (Fig. 6A). The pressure release at the frontal surface leads to the material movement in the directions perpendicular to the droplet, what results in the thermomechanical ablation of hot material in the heated layer. Here in this work we do not discuss the flow of ablated particles for the convenience of presenting the main simulation results related to experimental snapshots presented in Section "Evolution of droplet shape observed in experiments".

Hereafter, in order to analyze the material motion in droplets with different radii and demonstrate hydrodynamic similarity, we should use the dimensionless quantities of length and time: the distance from the center of a droplet along the polar axis is normalized to the droplet radius $x^* = x/R$, and the dimensionless time $t^* = ct/R$ is through the ratio of the sound propagation distance to the droplet radius.

The pressure wave formed due to material heating by irradiation begins to converge to the center of a droplet. Its profile along the radial direction has a typical triangular-like form, in which an unloading/rarefaction tail moves behind the leading shock front. The initial pressure pulse is very short and comparable with the heated depth, so its propagation is accompanied by spatial broadening and quite rapid decrease in its maximum pressure [36]. Thus, at the distance of $x/R \sim 0.2$ from the frontal surface (i.e. at the position $x/R \sim -0.8$), the pressure maximum of this wave decreases by a factor of ~ 2 and continues to fall gradually to 12 GPa at the distance of $x/R \approx 0.4$, see Fig. 7A. The tensile wave is characterized by a similar trend. Visually, the pressure wave broadening and the decrease of its maximum are also observed in the reduced pressure maps shown in Fig. 6B.

The gradual decrease of the pressure maximum during the wave convergence towards the center of a droplet changes with time to the gradual increase due to the focusing effect. Figure 7A shows that the pressure maximum begins to increase at a certain time, while the radial profile of the wave is broadening as before. The phenomenon occurs due to the localization of the strain energy within a smaller volume near the center of a droplet. As a result, the specific energy per unit mass increases and the pressure rises despite the fact of the radial wave broadening. Quantitatively, the shock wave amplitude increases from $P_{max} = 12\,$GPa at the dimensionless position $x/R \approx -0.6$ in the left part of droplet to $P_{max} = 20\,$GPa at $x/R \approx 0.1$ just after passing the center of a droplet, see Figs. 6C and 7A. The focusing effect is valid not only for compressions, but also for tensile stresses (Figs. 6C and 7A). The amplitude of the tensile wave $|P_{min}|$ increases in absolute value, and at the position $x/R = -0.4$ it reaches the spall strength of tin, which leads to the relaxation of tensile stresses via the formation of a central cavitation zone with multiple voids. Those voids increase in size and merge into a single large cavity nearby the center of a droplet with propagation of the tensile tail as shown in Fig. 6 and in the Supplemental Video at [URL will be given by publisher]. Figure 7A shows the left and right boundaries of the central cavitation zone on the polar axis.

Focusing of the strain energy nearby the center of a droplet is followed by the diverging pressure wave, which results in decreasing of its maximal pressure as seen in Figs. 6D and 7A. In particular, the shock-wave pressure decreases by an order of magnitude from 20 GPa nearby the center to $\sim 3\,$GPa at a position close to the rear side of a droplet (Figs. 6E, 7A, and 7B). Such decrease of amplitude is also applied to the tensile part of the diverging pressure wave. The tensile stress becomes lower than the spall strength of liquid tin at the relative position $x/R = 0.4 - 0.5$ what ceases the void formation and determines the right boundary of cavitation zone, see Figs. 6E and 7A.

Figure 7B shows the triangle pressure profile approaching the rear side of a droplet. Its maximum is $\sim 4\,$GPa and decreases linearly behind the front. The reflection of such pressure wave from the free rear-side boundary generates the reflected unloading wave propagating backward to the center of a droplet, which causes the material stretching by its tensile stress. The spallation condition is satisfied near the opposite pole as a result of superposition of the two tensile waves moving towards each other: the original tensile tail and the reflected unloading wave as illustrated by the arrows in Fig. 7C. As a result the rear-side cavity is formed, which is marked

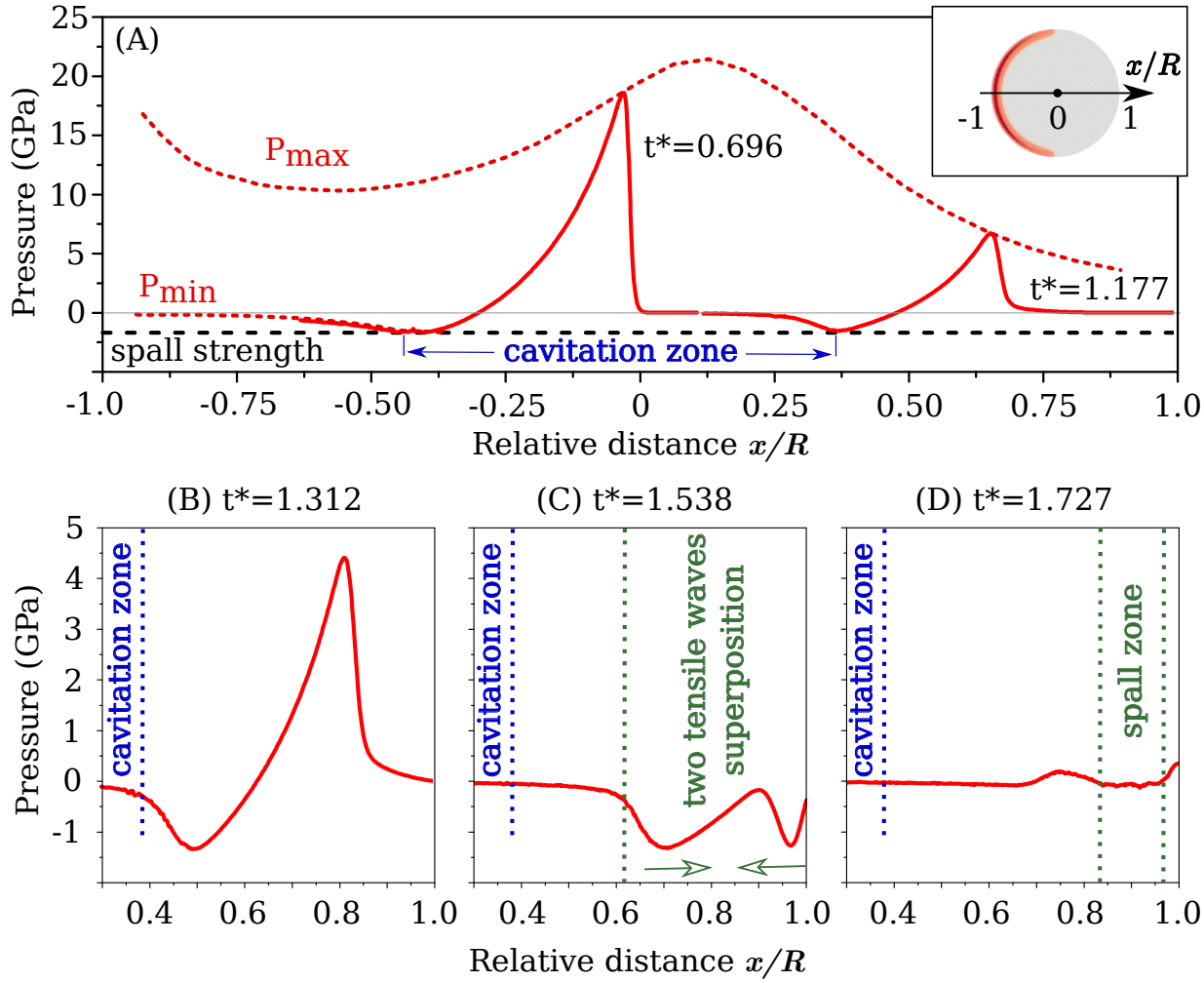

Figure 7. Evolution of the pressure profile along the polar (laser beam) axis: (top A) the cavity formation in the cavitation zone $x/R = (-0.5, 0.4)$ produced by the convergence of the pressure wave; (bottom B,C,D) the formation of the spallation zone at the rear surface of the droplet as a result of superposition of the two tensile waves moving towards each other: the coming to and the reflected from the free rear surface.

as the dashed right zone in Fig. 6F. The formation of spallation zone is accompanied by the tensile stress relaxation, which is represented by a light-blue color range with close-to-zero pressures in Fig. 6F. The surrounding bright blue-colored regions are under large, but not sufficient to form voids, tensile stresses. The rear-side spallation zone is narrower than the central cavitation zone because the required tensile stress could be generated only in a narrow region within the overlap of the two relatively weak tensile waves.

The central cavitation zone consists of an ensemble of many small voids. Their growth and merging form a single cavity surrounded by a liquid shell, which is expanding with time. Figure 8-1A shows the cavity with the radius $x/R \sim 0.5$ formed at the dimensionless time $t^* = 12.925$, what corresponds approximately to the linear x-size of area originally occupied by the small voids. Later at $t^* = 31.725$ the cavity radius becomes comparable with the initial radius of a droplet (Fig. 8-1C) and it continues to increase. At later stages, when the cavity exceeds the initial droplet radius significantly and the cavity shell becomes sufficiently thin, the further shell expansion and fragmentation are determined by the surface tension which is neglected in this work.

Effect of radiation intensity

The additional mechanism of fragmentation at relatively high laser intensities is associated with the spallation of rear-side material at the pole of a droplet opposite to the irradiated frontal side. Figure 8A shows that a thin liquid film is detached from the rear surface of a droplet as a result of spallation after shock-wave reflection. It should be noted that the spallation takes place in a thin zone under a relatively small surface area near the pole of a droplet only, because the incident pressure wave becomes weaker with approaching the equatorial zone, and

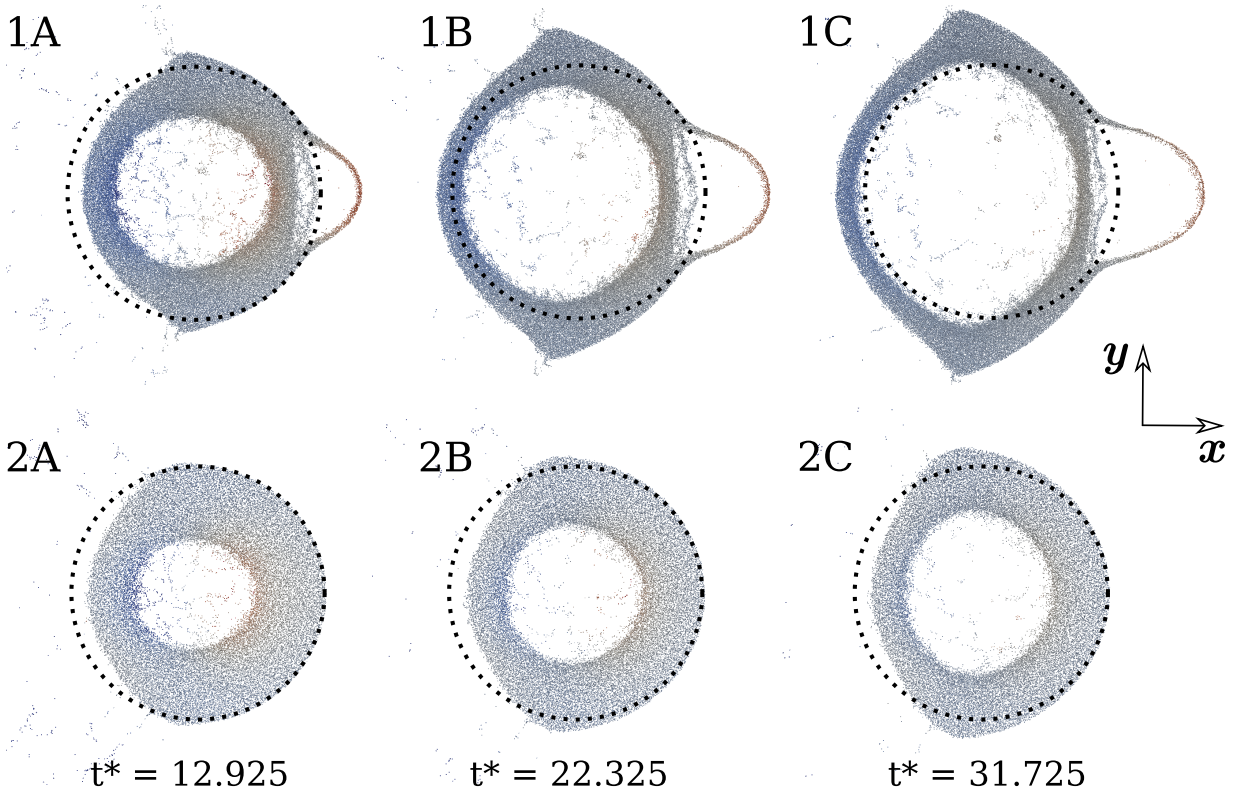

Figure 8. Two regimes of droplet evolution illustrated by mass distributions in a thin central cross-section slab. (1) the high-intensity regime: the growth of a large cavity at the center of a droplet as well as the rear-side spallation at the posterior pole are observed; (2) the moderate-intensity regime: the rear-side spallation does not occur, and the growth rate of a central cavity decreases. The evolution of mass distribution in the high-intensity regime is shown by shadowgraphs of the whole sample in Supplemental Video at [URL will be given by publisher].

the weakening tensile tail itself cannot initiate spallation as it was discussed in the preceding section.

Thus, there is a qualitative analogy between the results obtained in the simulations and the experimental data: Irradiation of a liquid-metal tin droplet with a short high-intensity laser pulse leads to the formation of two spatially separated shells. According to our analysis, the first shell of the central cavity emerges due to cavitation around the center of a droplet, whereas the second rear-side shell is formed as a result of spallation under the rear surface of a droplet.

The thickness of the central cavity shell is minimal on the rear and front sides and much wider in the equatorial region as seen in Fig. 8-1C. Thus, further expansion of the cavity shell should lead first to fragmentation of its frontal and rear-side parts. The thick equatorial "ring" around the polar axis should be more stable and fragment later. Such fragmentation sequence is confirmed by the experimental shadowgraphs presented in Figs. 2 and 3. The formation of a ring is exhibited for shadowgraphs taken at the angle of 30° to the horizontal projection of the laser beam (Fig. 3), what indirectly indicates that the emerging shell begins to break down at the poles of a droplet. The equatorial liquid ring can expand for a long time until it fragments into several small droplets via the Plateau–Rayleigh instability.

Lower laser intensity leads to a gradual suppression of both the cavitation and spallation at the center of a droplet and at the rear pole, respectively. The cavitation zone with a smaller volume is produced by a laser pulse with the twice lower intensity (Figs. 8-2A–8-2C). Moreover, the droplet shape evolution for decreasing intensities shown in Fig. 8 demonstrates a significant decrease in the cavity growth rate. At lower intensities the shells expansion rate becomes smaller what qualitatively agrees with the conclusions of the experiments. The intensity of cavitation and spall processes also decreases with the absorbed laser pulse energy. A decrease in the radiation intensity by a factor of 2 results in the drop of the shock-wave pressure to ~ 0.8 GPa near the rear pole of a droplet. Such weak shock wave cannot induce spallation after reflection. Thus, there is a threshold of the laser pulse intensity for the given droplet radius, below which the spallation cannot be developed for the given strain rate. Below this threshold the expansion and fragmentation of droplet are determined only by cavitation processes nearby the center.

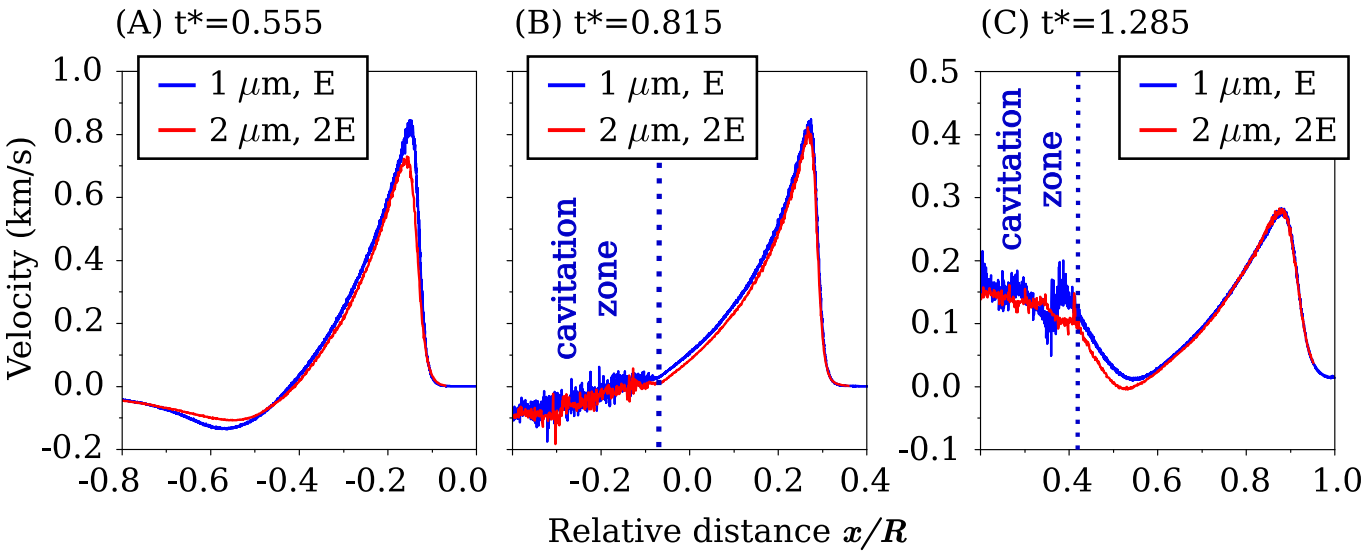

Figure 9. Velocity profiles along the laser beam axis: (A) before the formation of cavitation zones; (B) at the dimensionless time when the pressure wave passes through the center; and (C) at the moment of wave arrival to the rear-side surface. The comparison is given for droplets with radii $R = 1\,\mu$m (blue curve) and $R = 2\,\mu$m (red curve) with the correspondingly scaled energy densities q_m. Radial positions inside droplets are normalized to the corresponding radii.

Similarity in droplet expansion

The effect of the droplet size on expansion and fragmentation is studied using droplets with radii $R = 1\,\mu$m and $R = 2\,\mu$m. It should be noted that the problem of scaling effects is complex. First, the presser of the converging compression wave near the center of a droplet can increase with the droplet radius growth, because the total energy input rises. On the other hand, an increase in the size is accompanied by a large broadening of the wave profile, thereby reducing the shock-wave pressure. Thus, there are two competing processes, one of which contributes to the increase in the amplitude of the shock wave, while the other, on the contrary, to its decrease.

Hydrodynamic similarity is realized for different droplet sizes if the simultaneous scaling of spatial and temporal variables is performed in governing equations, boundary and initial conditions [37]. Thus, solutions for droplets of different sizes will be similar if the heated depths δ_h in them differ by the ratio of their radii. In addition, it is necessary to change similarly the size of the SPH particles to keep the perfect similarity in simulation. Such scaling conserves the total deposited energy per the droplet volume $Q_{tot}/R^3 = \text{const}$, where $Q_{tot} = \int q(\mathbf{r},t)\mathrm{d}V\,\mathrm{d}t \sim q_m R^2 \delta_h \tau$, hence $q_m\delta_h\tau/R = \text{const}$. On the other hand, for the given pulse duration τ and laser intensity I_L the total deposited energy is $Q_{tot} \sim \tau I_L R^2$, then the above scaling condition can be rewritten as:

$$\frac{I_L}{R} \sim \frac{q_m \delta_h}{R} = \text{const}. \qquad (7)$$

Comparison of velocity profiles along the polar axis obtained in simulations of droplets with radii $R = 1\,\mu$m and $R = 2\,\mu$m demonstrates the perfect similarity, see Appendix C. However, for the pulsed laser irradiation the heated depth is independent from the droplet size, which violates the perfect similarity just after the laser pulse, but we show below that the similarity is regained with time.

A pressure wave, generated as a result of an instantaneous heating, begins to forget its original profile after a considerable propagation distance from the thin heated surface layer where it was generated. Due to the fact that the initial width of pressure profile is about 100 nm, this width will increase by an order of magnitude at a relatively small propagation distance, because of the large sound velocity dispersion in the given range of compression. Therefore, even if there is a difference in the widths of initial pressure profiles, it will be leveled with distance. Thus, the micrometer-sized pressure profiles formed in the bulk of droplet will be asymptotically similar, and their integral characteristics are being preserved for the different heated layer depths varying within a few hundred nanometers.

We will rely on the above-mentioned fact that solutions for different droplets are similar according to Eq. (7). In the first approximation, it can be assumed for the given q_m used in Eq. (6) that an increase of the heated depth δ_h with the droplet radius R produces an effect similar to that produced by a proportional increase of q_m with R while maintaining the heated depth. Thus, the fragmentation scenarios of droplets, whose sizes are N times different, are expected to be identical if the laser-pulse intensities are also N times different.

A comparison of velocity profiles along the polar axis obtained in simulations of two droplets with radii $R = 1\,\mu$m (blue curve) and $R = 2\,\mu$m (red curve) is shown in Fig. 9. The absorbed energy q_m per unit mass is doubled

in simulation of droplet with $R = 2\,\mu$m, but the heated depth remains the same in both simulations. The constancy of the heated depth is justified, because its dependence on the laser pulse intensity is rather weak as shown in details in Appendix B. The velocity profiles are given for three different times: before the void formation and cavitation (Fig. 9A), as the shock front passes through the center of a droplet (Fig. 9B), and when the pressure wave approaches the rear side of droplet as shown in Fig. 9C. Thus, a good asymptotic similarity demonstrated here is close to the perfect similarity discussed above and in Appendix C.

Figure 9 shows a good coincidence of both the shock-wave fronts and the profiles of unloading tails. Because the spatial coordinate is normalized to the radius, the corresponding strain rate $du(x)/dx$ is two times lower in the droplet with $R = 2\,\mu$m than that in the droplet with $R = 1\,\mu$m. The greatest difference is observed in the stretching region. It is seen in Fig. 9(A) that the negative stresses for a smaller droplet are larger in magnitude. Thus, it can be expected that the void formation begins earlier for smaller droplets. However, the dependence of the spall strength on the strain rate can slightly improve the coincidence. The wave profiles remain similar when the waves approach the rear surface of a droplet; therefore, the conditions for rear-side spallation will be almost identical with the exception of the slightly different spall strengths.

In general, a good similarity of the wave profiles for droplets of different sizes suggests that the fragmentation described above for a droplet with $R = 1\,\mu$m will be similar for droplets of a larger size if Q_{tot}/R^3 is kept constant.

To quantitatively compare the simulation results with the experimental data, we estimate the total absorbed energy of laser irradiation per mass of a whole droplet as $3Q_{tot}/4\rho\pi R^3$. In the section describing the experimental setup, it is noted that the laser pulse intensity I_L varied in the range $(0.4 - 8.0) \times 10^{13}\,\mathrm{W/cm^2}$. This corresponds to the specific energy $q_{exp} = 3I\tau/4\rho R = (0.14 - 2.81) \times 10^6\,\mathrm{J/kg}$. At such laser intensities, the experimentally estimated velocity of the rear surface, which is carried away as a result of rear-side spallation, varies in the range from 100 to 500 m/s, see Fig. 4. In particular, at the specific energy $q_{exp} = 1.408 \times 10^6\,\mathrm{J/kg}$, the velocity of the rear surface is 300 m/s. The simulation of the droplet with $R = 2\,\mu$m gives the same rear-side velocity at the maximal absorbed energy $q_m = 7.5 \times 10^6\,\mathrm{J/kg}$ in the heated layer, which corresponds to the total absorbed energy per the droplet mass $q_{sim} = 0.176 \times 10^6\,\mathrm{J/kg}$. The ratio $q_{sim}/q_{exp} \cong 0.125$ can serve as an estimate of the absorption coefficient. The theoretically calculated absorption coefficient for liquid tin is $\sim 20\,\%$[38], which is close to the above estimate.

Figure 4 compares the expansion rates/velocities of the central and rear-side shells, which were measured in experiments and obtained from simulations for the different irradiation intensities, where the top axis shows the total absorbed energy normalized per the droplet mass. The circles in Fig. 4 denote the transverse expansion velocity of the central shell, and the squares – the rate of expansion of the rear-side shell in the longitudinal direction along the laser beam axis. It can be seen that the experimentally measured expansion rate of the rear-side shell increases with the irradiation intensity growth much faster than in the central shell, which indicates different mechanisms of their formation. The corresponding velocities (blue colored symbols in Fig. 4) obtained in our simulations show a similar behavior. There is good agreement between many shell velocities from simulations and the experimentally observed velocities if a constant absorption coefficient is set to 0.125.

CONCLUSIONS

We have studied experimentally and numerically the expansion and fragmentation of a liquid-metal droplet irradiated by a short laser pulse. The fast energy deposition heats and pressurizes material within a thin frontal layer of a droplet in the almost isochoric regime. The propagation of a laser-generated pressure wave and physical mechanisms of fragmentation at various laser pulse energies are examined in detail.

It is found in SPH simulation that the fragmentation of a droplet is triggered by the increasing tensile stress produced in an unloading wave following the leading shock-wave front moving towards the center of a droplet. As a result of unloading wave convergence, the central cavitation zone is formed nearby the center. For the higher laser pulse energies the second cavity can be formed at the rear surface as a result of spallation of a thin rear-side shell after reflection of the shock wave from the free boundary of a droplet.

Two fragmentation regimes have been experimentally demonstrated. It has been shown both in experiments and simulations that at a high intensity two spatially separated shells are formed, one of which is a central spherical shell surrounding the central cavity, another is a rear-side shell spalled from the rear side of a droplet. The expansion of those shells leads to the fragmentation of a droplet. Only a single central shell is formed in the low-intensity regime, at which the expansion and subsequent fragmentation of a droplet becomes more symmetrical in comparison with the high-intensity regime.

We have shown the existence of a critical intensity of the laser light below which the spallation nearby the rear side of a droplet does not develop. It has been shown in a simulation that the fragmentation pattern is preserved for droplets of different sizes, provided that the absorbed energy of the laser pulse per the total droplet mass remains constant.

ACKNOWLEDGMENTS

The works of S.Yu.G., V.V.Z., S.A.D, D.K.I, K.P.M. and N.A.I. were supported by the Russian Science Foundation grant 14-19-01599.

APPENDIX A: ELECTRON–ION EXCHANGE COEFFICIENTS AND ELECTRONIC THERMAL CONDUCTIVITY

Quantum molecular dynamics (QMD) simulations are performed for tin in the cubic supercell containing 64 atoms with the periodic boundary conditions. The cube face size is 1.28 nm which corresponds to the density of 6.05 g/cm^3. The simulation time step is 1 fs. There are 3 stages of simulation:

1. 1000 steps using the NVT thermostat with an increase in temperature from 300 to 4000 K in order to accelerate the melting;

2. 1000 steps using the NVT thermostat with cooling from 4000 to 1000 K;

3. 300 steps using the NVE ensemble (without the thermostat) to make sure that the final state is stable and remains liquid during the simulation lasting 2-3 ps.

The effect of the semi-valence 4d electrons on the interatomic interaction is correctly taken into account by using the PAW pseudopotential which considers these electrons to be valence. The pseudopotential is a part of the library within the VASP software [39, 40]. The effects of the electronic exchange and correlation are taken into account in the framework of the generalized gradient approximation (PBE) [41]. The electronic structure is calculated for a single Γ-point using 544 blank electronic states per cell and the PAW cutoff energy 260 eV.

The averaging over the last 60 configurations obtained in the 3d stage provides the electronic density of states (DOS) in liquid tin which is parabolic in the region near the Fermi energy. Similarly, the DOS computed for tin at the equilibrium temperatures of 2000, 4000, and 8000 K has no significant difference from the one obtained at 1000 K.

In addition, we conducted a test to determine the effect of the electronic temperature on DOS. The unit cell of α-tin with the ion density of 6.05 g/cc is considered. Electron temperatures to test are 10 000, 20 000, 45 000, and 55 000 K. The electronic exchange and correlation are taken again in the generalized gradient approximation (PBE) [41]. Additional adjustments are the $21 \times 21 \times 21$ wave-vector mesh constructed by the Monkhorst–Pack algorithm, the plane-wave cutoff energy was 300 eV, and the unfilled electronic states number per atom equals to 32. The performed tests do not demonstrate noticeable dependence of tin DOS from the electronic temperature.

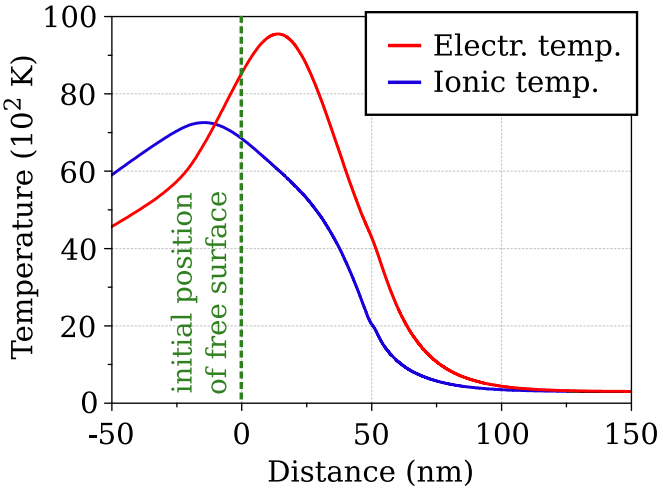

Figure 10. Temperature distribution of electrons and ions in 10 ps after laser pulse irradiation.

The two-parabolic approximation [42] which takes into account the presence of a semi-valence 4d band is used for further calculations. The sp-electron band is described by a parabola with the energy minimum of −10.7 eV and the effective electron mass of 0.83 in vacuum. The two-parabolic DOS of tin is used to obtain electronic thermodynamic characteristics. The expression for the electronic heat capacity (measured in 10^5 J/m^3/K):

$$C_e = 1 + 4.64 \times 10^{-4}\, T_e + 3.1 \times 10^{-9}\, T_e^2, \qquad (8)$$

remains valid according to calculations with the two-parabolic DOS up to 100 000 K. The role of d-electrons below −20.5 eV with respect to the Fermi energy manifested itself in a moderate increase in the thermal conductivity at T_e above 30 000 K, which was already obtained for tungsten [43]. The electronic temperature T_e in this and further expressions is given in K. The same applicability threshold corresponds to the obtained expressions for the electron internal energy density (in GPa):

$$u_e = 0.54 - 4.47 \times 10^{-6}\, T_e + 3.0 \times 10^{-8}\, T_e^2, \qquad (9)$$

and the electron pressure:

$$P_e = 5.785 \times 10^{-5}\, T_e + 2.462 \times 10^{-8}\, T_e^2. \qquad (10)$$

The effect of electron–electron collisions in the two-temperature electron thermal conductivity is taken into account in accordance with the modification [44] of the approach [42], where the loss of conducting properties is considered due to the increasing losses for thermoelectric phenomena at T_e = 30 000 – 50 000 K. The form, proposed by Lindhard, is used to describe the electronic screening. The final expression for the contribution of s–s collisions to the total effective frequency of electron collisions (in units of s^{-1}) has the form:

$$\nu_{ss} = \left(\sqrt{(8 \times 10^{-5}\, T_e)^2 + 0.49} - 0.7 \right) \times 10^{15}. \qquad (11)$$

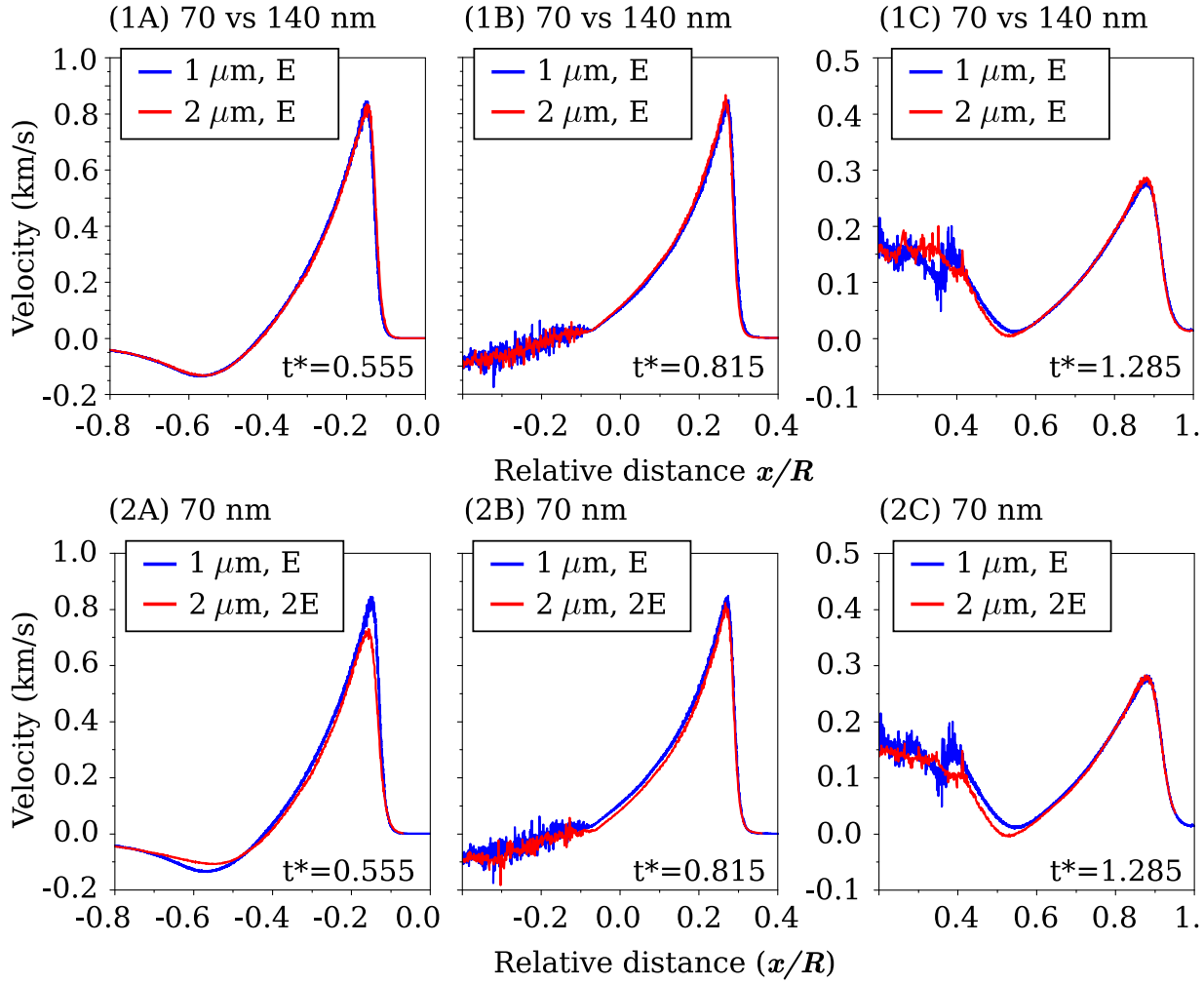

Figure 11. (1A)–(1C): complete similarity of velocity profiles with a simultaneous change of time scale and all scales of length: droplet size, heating depth, and size of SPH particles; (2A)–(2C): incomplete (asymptotic) similarity of velocity profiles for droplets of various sizes while maintaining the heating depth and the specific absorbed energy per entire mass of a droplet.

Analysis of the experimental data [45, 46] using the Drude model yields the following estimation of the effective frequency of electron–ion collisions in tin:

$$\nu_{si} = \frac{3\times10^{14}\,T_i}{36+0.09\,T_i}. \qquad (12)$$

Here the ionic temperature T_i is given in Kelvins too. The final expression for the electronic thermal conductivity (in W m/K) is also obtained using the Drude model. The s and p–electrons are considered as charge and energy carriers used in the two-parabolic approximation:

$$\kappa_e = \frac{C_s V_s^2}{3(\nu_{si}+\nu_{ss})}. \qquad (13)$$

The sp–electron velocity $V_s = 3\times10^{14}\,T_e$ (in SI units).

The electron–phonon heat exchange is described using the approach [42], where the experimental sound speed of 2.4 km/s in liquid tin [47] is utilized. The approximating expression is:

$$\alpha = 0.41 + 1.91\times10^{-8}\times T_e + 3.64\times10^{-11}\,T_e^2, \qquad (14)$$

which is given in units of 10^{17} W/K/m^3. Calculations are verified using the well-known Allen method [48] where $\lambda = 0.6$ [49] and the mean square of the oscillation frequency of acoustic phonons $\langle\omega^2\rangle$ are used for the electron-phonon coupling constant on the experimental data basis [50]. The resulting value of $\lambda\langle\omega^2\rangle$ used in the Allen formula is 19 MeV. The obtained value of electron-phonon heat transfer at electron temperatures up to 10 000 K is 0.25×10^{17} W/K/m^3.

APPENDIX B: 2T HYDRODYNAMICS

The system of equations for the two-temperature hydrodynamics is solved numerically to estimate the heated layer depth δ_h in tin. The nonequilibrium process of heat-

ing the electronic subsystem of the material and its further relaxation are taken into account. In the Lagrangian coordinates $dm = \rho dx$, the energy balance is divided into two independent equations for the electronic and ionic subsystems:

$$\frac{\partial \epsilon_e}{\partial t} + P_e \frac{\partial u}{\partial m} = \frac{\partial}{\partial m}\left(\kappa_e \rho \frac{\partial T_e}{\partial m}\right) - \frac{\alpha}{\rho}(T_e - T_i) + J_L, \quad (15)$$

$$\frac{\partial \epsilon_i}{\partial t} + P_i \frac{\partial u}{\partial m} = \frac{\alpha}{\rho}(T_e - T_i), \quad (16)$$

where ϵ, P, T are the internal energy, the pressure and the temperature, respectively, for the electronic (subscript e) or ionic (subscript i) subsystems; α is the coefficient of the electron–ion heat transfer, κ_e is the coefficient of the electronic thermal conductivity which is determined using QMD simulations. Material motion in one-dimensional hydrodynamics is described via the energy balance equations (15)–(16) which are supplemented by the equations of continuity momentum balance and the equation of state for the ionic post-system. The laser energy J_L absorbed by a unit mass per unit time is represented in the form:

$$J_L = \frac{F_{abs}}{\tau \delta \sqrt{\pi} \rho} \exp\left(-\frac{t^2}{\tau^2}\right) \exp\left(-\frac{x - x_0}{\delta}\right), \quad (17)$$

where F_{abs} is the laser energy, absorbed by the unit of the irradiated surface, $\delta \approx 8.5\,\text{nm}$ is the thickness of skin layer in tin, $x = x(m,t)$ and $x_0 = x(m_0,t)$ are the trajectories of lagrangian particles with coordinates m and m_0, m_0 is the lagrangian coordinate of the metal surface on which the light is incident, and τ is the laser pulse duration.

A series of calculations is performed to estimate the heating depth. As a result, it varies from 60 to 80 nm over a wide range of fluences. Figure 10 shows the distribution of the electron and ion temperatures at 10 ps after irradiation by a 800-fs laser pulse with the energy flux of $1\,\text{J/cm}^2$.

APPENDIX C: ANALYSIS OF SIMILARITY

A complete similarity in the evolution of irradiated droplets of various sizes is shown for two droplets with $R = 1\,\mu\text{m}$ and $R = 2\,\mu\text{m}$. The heated depths δ_h are 70 and 140 nm for the first and the second case, respectively. In addition to physical dimensions it is necessary to change the mesh size properly. Figures 11-1A–11-1C demonstrate the velocity profiles at different dimensionless times for those two droplets. The position x/R is normalized by a droplet radius, and the origin corresponds to the center of a droplet. The obtained profiles are practically identical as expected.

Such perfect similarity in the evolution of droplets after absorbtion of the same specific energy Q_{tot}/R^3 in a fixed heated depth cannot be realized. However, our simulations demonstrate that the asymptotic similarity is established when the wave profiles move to large enough distances from the heated surface layer as shown in Figs. 11-2A–11-2C. There the velocity profiles in the reduced coordinates are very close for waves approaching the center of a droplet. There is only a small difference appearing in the cavitation zone. Such asymptotic similarity persists even when the diverging pressure wave approaches the rear-side surface of droplet as seen in Fig. 11-2C.

[1] E. Villermaux and B. Bossa, Nature Physics **5**, 697 (2009).
[2] J. Sherwood, Journal of Fluid Mechanics **188**, 133 (1988).
[3] J. S. Eow, M. Ghadiri, and A. Sharif, Journal of Electrostatics **51**, 463 (2001).
[4] D. Guildenbecher, C. López-Rivera, and P. Sojka, Experiments in Fluids **46**, 371 (2009).
[5] E. Villermaux and B. Bossa, Journal of Fluid Mechanics **668**, 412 (2011).
[6] Y. Pan and K. Suga, Physics of Fluids **17**, 082105 (2005).
[7] A. L. Klein, W. Bouwhuis, C. W. Visser, H. Lhuissier, C. Sun, J. H. Snoeijer, E. Villermaux, D. Lohse, and H. Gelderblom, Phys. Rev. Applied **3**, 044018 (2015).
[8] V. Boiko and S. Poplavskii, Fluid Dynamics **42**, 433 (2007).
[9] V. Boiko and S. Poplavski, Combustion, Explosion, and Shock Waves **48**, 440 (2012).
[10] J. E. Field, J. P. Dear, and J. E. Ogren, Journal of Applied Physics **65**, 533 (1989).
[11] C. A. Stan, P. R. Willmott, H. A. Stone, J. E. Koglin, M. Liang, A. L. Aquila, J. S. Robinson, K. L. Gumerlock, G. Blaj, R. G. Sierra, S. Boutet, S. A. H. Guillet, R. H. Curtis, S. L. Vetter, H. Loos, J. L. Turner, and F.-J. Decker, The Journal of Physical Chemistry Letters **7**, 2055 (2016).
[12] A. Lindinger, J. Hagen, L. D. Socaciu, T. M. Bernhardt, L. Wöste, D. Duft, and T. Leisner, Appl. Opt. **43**, 5263 (2004).
[13] M. S. Krivokorytov, A. Y. Vinokhodov, Y. V. Sidelnikov, V. M. Krivtsun, V. O. Kompanets, A. A. Lash, K. N. Koshelev, and V. V. Medvedev, Phys. Rev. E **95**, 031101 (2017).
[14] M. M. Basko, M. S. Krivokorytov, A. Y. Vinokhodov, Y. V. Sidelnikov, V. M. Krivtsun, V. V. Medvedev, D. A. Kim, V. O. Kompanets, A. A. Lash, and K. N. Koshelev, Laser Physics Letters **14**, 036001 (2017).
[15] A. Y. Vinokhodov, K. N. Koshelev, V. M. Krivtsun, M. S. Krivokorytov, Y. V. Sidelnikov, V. V. Medvedev, V. O. Kompanets, A. A. Melnikov, and S. V. Chekalin, Quantum Electronics **46**, 23 (2016).
[16] M. S. Krivokorytov, Q. Zeng, B. V. Lakatosh, A. Y. Vinokhodov, Y. V. Sidelnikov, V. O. Kompanets, V. M.

Krivtsun, K. N. Koshelev, C. D. Ohl, and V. V. Medvedev, Scientific reports **8**, 597 (2018).
[17] D. Kurilovich, T. d. F. Pinto, F. Torretti, R. Schupp, J. Scheers, A. S. Stodolna, H. Gelderblom, K. S. E. Eikema, S. Witte, W. Ubachs, R. Hoekstra, and O. O. Versolato, arXiv:1805.07283 [physics.flu-dyn] (2018).
[18] J. Fujimoto, H. Mizoguchi, T. Abe, S. Tanaka, T. Ohta, T. Hori, T. Yanagida, and H. Nakarai, Journal of Micro/Nanolithography, MEMS, and MOEMS **11**, 021111 (2012).
[19] I. Fomenkov, D. Brandt, A. Ershov, A. Schafgans, Y. Tao, G. Vaschenko, S. Rokitski, M. Kats, M. Vargas, M. Purvis, *et al.*, Advanced Optical Technologies **6**, 173 (2017).
[20] V. V. Medvedev, A. S. Grushin, V. M. Krivtsun, A. Y. Vinokhodov, P. S. Antsiferov, M. S. Krivokorytov, D. I. Astakhov, D. B. Abramenko, L. A. Dorokhin, E. P. Snegirev, O. F. Yakushev, B. V. Lakatosh, R. R. Gayazov, A. D. Solomyannaya, I. P. Tsygvintsev, D. A. Kim, Y. V. Sidel'nikov, A. A. Yakushkin, A. A. Lash, A. N. Ryabtsev, and K. N. Koshelev, Phys. Usp. , in press (2018).
[21] S. Fujioka, M. Shimomura, Y. Shimada, S. Maeda, H. Sakaguchi, Y. Nakai, T. Aota, H. Nishimura, N. Ozaki, A. Sunahara, *et al.*, Applied Physics Letters **92**, 241502 (2008).
[22] D. Kurilovich, A. L. Klein, F. Torretti, A. Lassise, R. Hoekstra, W. Ubachs, H. Gelderblom, and O. O. Versolato, Phys. Rev. Applied **6**, 014018 (2016).
[23] R. A. Gingold and J. J. Monaghan, Monthly Notices of the Royal Astronomical Society **181**, 375 (1977).
[24] J. Monaghan, Journal of Computational Physics **136**, 298 (1997).
[25] A. N. Parshikov and S. A. Medin, J. Comp. Phys. **180**, 358 (2002).
[26] M. S. Egorova, S. A. Dyachkov, A. N. Parshikov, and V. V. Zhakhovsky, Computer Physics Communications **234**, 112 (2019).
[27] M. J. Assael, A. E. Kalyva, K. D. Antoniadis, R. Michael Banish, I. Egry, J. Wu, E. Kaschnitz, and W. A. Wakeham, Journal of Physical and Chemical Reference Data **39**, 033105 (2010).
[28] M. J. Assael, I. J. Armyra, J. Brillo, S. V. Stankus, J. Wu, and W. A. Wakeham, Journal of Physical and Chemical Reference Data **41**, 033101 (2012).
[29] *LASL Shock Hugoniot Data* (University of California Press, Berkley, 1980) pp. 245–246, edited by S. P. March.
[30] V. I. Kononenko, S. P. Yatsenko, and A. L. Sukhman, Zhur. Fiz. Khim. **46**, 1589 (1972).
[31] G. I. Kanel, A. S. Savinykh, G. V. Garkushin, and S. V. Razorenov, JETP letters **102**, 548 (2015).
[32] S. I. Ashitkov, P. S. Komarov, A. V. Ovchinnikov, E. V. Struleva, and M. B. Agranat, JETP Letters **103**, 544 (2016).
[33] D. Grady, Journal of the Mechanics and Physics of Solids **36**, 353 (1988).
[34] G. Kanel, S. Razorenov, A. Utkin, and D. Grady, in *AIP Conference Proceedings*, Vol. 370 (AIP, 1996) pp. 503–506.
[35] T. De Rességuier, L. Signor, A. Dragon, M. Boustie, G. Roy, and F. Llorca, Journal of applied physics **101**, 013506 (2007).
[36] D. E. Grady, L. Davison, and M. Shahinpoor, *High-Pressure Shock Compression of Solids II* (Springer, 1996).
[37] Y. B. Zel'Dovich and Y. P. Raizer, *Physics of shock waves and high-temperature hydrodynamic phenomena* (Academic Press, 1967) p. 505.
[38] E. Siegel, Physics and Chemistry of liquids **5**, 9 (1976).
[39] G. Kresse and J. Furthmüller, Phys. Rev. B **54**, 11169 (1996).
[40] G. Kresse and J. Furthmüller, Comput. Mat. Sci. **6**, 15 (1996).
[41] J. P. Perdew, K. Burke, and M. Ernzerhof, Phys. Rev. Lett. **77**, 3865 (1996).
[42] Y. V. Petrov, N. A. Inogamov, and K. P. Migdal, JETP Lett. **97**, 20 (2013).
[43] P. R. Levashov, G. V. Sin'ko, N. A. Smirnov, D. V. Minakov, O. P. Shemyakin, and K. V. Khishchenko, J. Phys.: Cond. Mat. **22**, 505501 (2010).
[44] K. Migdal, D. Il'nitsky, Y. Petrov, and N. Inogamov, J. of Phys.: Conf. Ser. **653**, 012086 (2015).
[45] I. Savchenko, S. V. Stankus, and A. S. Agadjanov, High Temperature **49**, 506 (2011).
[46] A. B. Patel, N. K. Bhatt, B. Y. Thakore, P. R. Vyas, and A. R. Jani, Molecular Physics **112**, 2000 (2014).
[47] S. Hosokawa, S. Munerji, M. Inui, Y. Kajihiri, W.-C. Pilgrim, Y. Ohmas, S. Tsutsui, A. Q. R. Baron, F. Shimojo, and K. Hoshino, J. Phys.: Condens. Matter **25**, 112101 (2013).
[48] Z. Lin, L. V. Zhigilei, and V. Celli, Phys. Rev. B **77**, 075133 (2008).
[49] W. L. McMillan, Phys. Rev. **167**, 331 (1968).
[50] K. J. Chang and M. L. Cohen, Phys. Rev. B **34**, 4552 (1986).